

See discussions, stats, and author profiles for this publication at: <https://www.researchgate.net/publication/330899304>

Proper orthogonal decomposition and dynamic mode decomposition of jet in channel crossflow

Article in Nuclear Engineering and Design · April 2019

DOI: 10.1016/j.nucengdes.2019.01.015

CITATIONS

16

READS

477

4 authors, including:



Dominique Laurence
The University of Manchester
145 PUBLICATIONS 3,986 CITATIONS

[SEE PROFILE](#)



Sergey Utyuzhnikov
The University of Manchester
173 PUBLICATIONS 1,529 CITATIONS

[SEE PROFILE](#)



Imran Afgan
The University of Manchester
48 PUBLICATIONS 711 CITATIONS

[SEE PROFILE](#)

Some of the authors of this publication are also working on these related projects:



Conference [View project](#)



Advanced Virtual Prototyping for Sustainable Energy Generation [View project](#)

Wu, Z.*; Laurence, D.; Utyuzhnikov, S.; Afgan, I. Proper orthogonal decomposition and dynamic mode decomposition of jet in channel crossflow.

Nuclear Engineering and Design, vol. 344, pp 54-68, 2019.

Proper Orthogonal Decomposition and Dynamic Mode Decomposition of Jet in Channel Crossflow

Zhao Wu^{a,*}, Dominique Laurence^a, Sergey Utyuzhnikov^{a,b}, Imran Afgan^a

^a*Modelling and Simulation Centre, School of Mechanical, Aerospace and Civil Engineering,*

The University of Manchester, Manchester M13 9PL, UK

^b*Moscow Institute of Physics and Technology, Dolgoprudny, 141700, Russia*

Abstract

The paper is devoted to the application of the model order reduction to the results of direct numerical simulation of a low momentum laminar jet discharged into a laminar channel crossflow through a circular orifice (Reynolds number $Re = 3333$, jet-to-crossflow velocity ratio is $R = 1/6$, mesh 13 million nodes, (Wu *et al.*, 2017a)). Main attention is paid to the post-processor analysis of the computational results via model order reduction techniques: the Proper Orthogonal Decomposition (POD) and Dynamic Mode Decomposition (DMD) which can drastically reduce the amount of data needed. Up to 400 snapshots, obtained by direct numerical simulation, are used to extract the structures. We study the sensitivity of both algorithms to the sampling frequency and time span. For the first time different DMD ranking approaches are analysed in the application to a low-dimensional flow reconstruction. It is shown that the DMD approach with the ranking with respect to the amplitudes averaged over time is the most efficient technique for the problem in study. A comparative analysis is also carried out for both POD and DMD. It is shown the energy is more evenly distributed in the DMD. In turn, the POD is quite optimal in reconstructing the flow while the DMD requires more modes to capture the same amount of energy. However, DMD modes automatically reveal the frequency information and corresponding spatial structures in the entire field as well as interactions between different parts of the flow domain.

Keywords: DMD; POD; Jet in crossflow

1. Introduction

The jet in crossflow (JICF) is of great industrial interest with applications in turbine blades film cooling, de-icing of aeroplane wings, power plant piping systems and pollutant into water or atmosphere. There is a number of experimental (Sherif and Pletcher, 1989; Fric and Roshko, 1994; Iacovides *et al.*, 2005; Shan and Dimotakis, 2006), theoretical (Coelho and Hunt, 1989; Cortelezzi and Karagozian, 2001) and numerical (He *et al.*, 1999; Muppudi and Mahesh, 2007; Rana *et al.*, 2011; Esmaeili *et al.*, 2015) studies. However, only a few papers (Andreopoulos,

*Corresponding author

Email address: zhao.wu@manchester.ac.uk (Zhao Wu)

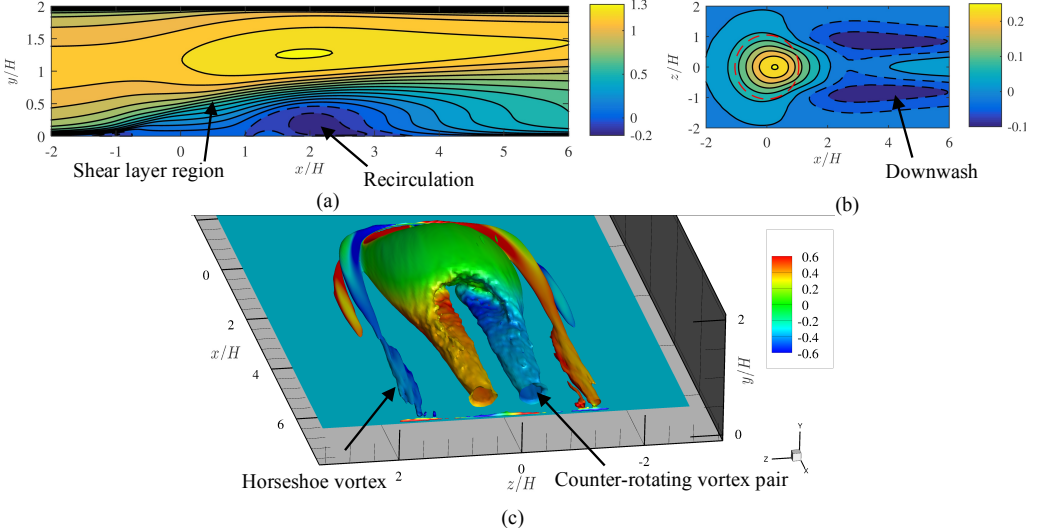


Figure 1: Time-averaged profiles in the turbulent crossflow case: (a) streamwise velocity $\langle u \rangle$ on the symmetry plane ($z/H = 0$); (b) normal velocity $\langle v \rangle$ on $y/H = 0.60$ plane; and (c) iso-surface of Q-criterion ($Q = 0.5$) coloured by the streamwise vorticity ω_x . The black dashed contour lines in (a) and (b) indicate the negative value. The red dashed circle in (b) indicate the jet-exit location.

1984; Tyagi and Acharya, 2003; Bidan and Nikitopoulos, 2013a) are focused on the jet in crossflow problems at a low jet-to-crossflow velocity ratio R which occur e.g. in T-junction pipes of
10 a nuclear power plant in emergency cooling systems. These flows are largely characterised by coherent structures with segregated spatial and temporal scales.

Time-averaged structures of a jet in crossflow at a low jet-to-crossflow velocity ratio R are depicted in figure 1. The crossflow partially covers the jet fluid, and they are connected by the shear layer. The horseshoe vortex forms at the front edge of jet-exit where the crossflow boundary
15 layer encounters the jet fluid. A counter-rotating vortex pair is seen in the wake region. The existence of multiple dominant structures in this fluid flow makes detection of the spatial-temporal features of each coherent structure challenging. Such identification, however, plays a significant role in the study of various physical processes, e.g., heat and mass transfer, and flow noise. Among
20 all of the data-driven algorithms that have been used to determine the features of vortices which are usually buried under turbulent flows, the proper orthogonal decomposition (POD) and the dynamic mode decomposition (DMD) have enjoyed widespread use.

The POD was brought to the fluid dynamics first by Lumley (Lumley, 1967). The POD takes as an expansion basis of the eigenvectors of the autocovariance matrix (computed from
25 the snapshots) and ranks the modes according to their energy content. Meyer *et al.* (Meyer et al., 2007) used POD to analyse a jet in boundary layer crossflow. They considered the jet-to-crossflow velocity ratios R equal to 1.3 and 3.3. They found the shear layer vortices are a more dominant flow feature at the lower velocity ratio while the wake vortices are more dominant at the higher velocity ratio. Bidan & Nikitopoulos (Bidan and Nikitopoulos, 2013b) applied POD
30 to film-cooling LES snapshots. It was shown that as the ranking of POD modes is entirely based on the kinetic energy contained in the modes, POD modes include flow structures with different

spectral information.

An alternative method based on the Koopman operator has emerged in the work of Rowley *et al.* (Rowley et al., 2009). The infinite-dimensional Koopman mode can be reduced and approximated using the DMD algorithm proposed by Schmid (Schmid, 2010). The DMD decomposes the dynamical system into a series of approximated Koopman modes. Contrary to the POD, the DMD modes are based on their dynamics rather than the energy content. A POD mode may contain a continuous frequency spectrum, while each DMD mode is characterized by a single frequency. This is a major difference between the two methods by nature. Thus, the DMD can be efficient in the identification of dominant frequencies. Sometimes if a flow structure contains relatively small energy, but is strongly connected with other structures sharing the same frequency, this structure is likely to be ignored by POD analysis but would be captured by the DMD. The POD modes are always orthogonal in space while it is not the case for DMD modes.

DMD is proved to be able to capture the dominant frequencies and spatial structures accurately (Rowley et al., 2009). Rowley *et al.* (Rowley et al., 2009) applied DMD to a parabolic jet in laminar boundary layer crossflow problem with a high jet-to-crossflow velocity ratio ($R = 3$). They showed the DMD can identify the spectral and spatial information of coherent structures automatically and globally. The method decouples and isolates the flow dynamics with different frequencies. Iyer & Mahesh (Iyer and Mahesh, 2016) used DMD to analyse the instability of the shear layer in the jet in boundary layer crossflow with $R = 2$ and 4. They also found the shear layer was the dominant structures in both cases.

However, in the above POD/DMD studies, the choice of the sampling frequency and the time span of the snapshots used in the DMD/POD analysis is not justified. One should expect that both parameters influence the flow structures extracted from POD/DMD. In contrast, we consider the sensitivity analysis and study the effect of time step and time span for both POD and DMD. Main attention is paid to the recognition of large scale structures driven by the flow. For the first time, we also carry out a low dimensional flow reconstruction based on different DMD ranking techniques to identify the most efficient approach for the problem in study.

The present study uses the POD and DMD to investigate the flow structures of the jet in channel crossflow at a low jet-to-crossflow velocity ratio R using the direct numerical simulation (DNS) results. This is a part of a numerical simulation research programme on the jet in channel crossflow at a low R , including (i) the discussion of the DNS configurations and flow physics (Wu et al., 2017b), (ii) DNS of conjugate heat transfer in jet in channel crossflow (Wu et al., 2017c) and (iii) the analysis of the flow structures using POD and DMD in this manuscript. Part of the DNS database is published online for public open access at <http://dx.doi.org/10.17632/7nx4prgjzz.3> (Wu et al., 2017a).

This paper is organized as follows. Sections 2 and 3 briefly describe the numerical details of POD and DMD, respectively. The flow configurations and the energy information in the POD and DMD modes are introduced and discussed in Section 4. A sensitivity analysis is also carried out for both POD and DMD algorithms. Sections 5 and 6 are devoted to the results obtained with POD and DMD approaches, respectively. A low-dimensional flow reconstruction is considered in Section 6 with the use of different DMD techniques introduced in Section 3. Finally, conclusions are given in Section 7.

2. Proper orthogonal decomposition

The POD is able to provide the most optimal low-ranking decomposition with respect to the energy content.

Consider a set of velocity values \mathbf{u} measured at N space points: $\mathbf{u} \in \mathbb{R}^{3N}$. Presume that there are M measurements. They can be stored in matrix

$$\mathbf{D} = [\mathbf{u}_1, \mathbf{u}_2, \dots, \mathbf{u}_M], \quad (1)$$

having a dimension $(3N \times M)$.

The POD can provide an approximation of the set of data \mathbf{D} in $\mathbb{R}^{3N \times M}$ such that the error is minimal in the Euclidean norm. To realize a robust approximation, it is much more efficient to place the centre of the coordinate system at the centre of the set or “cloud”. This can be achieved by subtracting the mean vector from each column of matrix D . In other words, the centre of the new coordinate system should be shifted by the mean vector. This can mean consideration of snapshots of velocity fluctuations instead of full velocities. Then, instead of matrix \mathbf{D} , we consider matrix:

$$\mathbf{D}' = [\mathbf{u}'_1, \mathbf{u}'_2, \dots, \mathbf{u}'_M], \quad (2)$$

where \mathbf{u}'_j is a j th fluctuating velocity snapshot.

The original POD can be realized via the standard Singular Value Decomposition (SVD). With the SVD one can present matrix \mathbf{D}' :

$$\mathbf{D}' = \mathbf{U}\Sigma\mathbf{V}^T, \quad (3)$$

where \mathbf{U} and \mathbf{V} are unitary matrices with dimension $(3N \times M)$ and $(M \times M)$, respectively. In
80 turn, matrix Σ is a diagonal $(M \times M)$ matrix with non-negative real numbers on the diagonal, which are called the singular values of matrix \mathbf{D}' . More precisely, the diagonal elements consist of $r = \text{rank}(\mathbf{D}')$ positive numbers $\sigma_j > 0$, $j = 1, 2, \dots, r$. Here, we suppose that the diagonal elements are numerated in the non-increasing order. The columns of matrix \mathbf{U} are called the modes while the squared diagonal elements σ_j define how much “energy” is in each mode. In
85 general, the columns of matrix \mathbf{U} contain key information on the spatial structures while the columns of matrix \mathbf{V} representing the temporal evolution.

The SVD can be calculated by means of solving an eigenvalue problem for both matrices $\mathbf{D}'\mathbf{D}'^T$ and $\mathbf{D}'^T\mathbf{D}'$. In practice, it is usually $M \ll N$. Then, since we are only interested in the r modes, it is much more efficient to consider the eigenvalue problem only for matrix $\mathbf{D}'^T\mathbf{D}'$
90 with much lower dimension of the two. Such an approach leads to the method of snapshots by Sirovich([Sirovich, 1987](#)).

In this way we arrive at the auto-covariance matrix:

$$\mathbf{C} = \frac{1}{M} \mathbf{D}'^T \mathbf{D}', \quad (4)$$

and the eigenvalues ξ_j and eigenvectors \mathbf{A}_j of \mathbf{C} are found as

$$\mathbf{C}\mathbf{A}_j = \xi_j \mathbf{A}_j, \quad (5)$$

where $j = 1, 2, \dots, r$. The numeration is given such that

$$\xi_1 \geq \xi_2 \geq \dots \geq \xi_r > 0. \quad (6)$$

It is easy to show that $\xi_j = \sigma_j^2/M$ ($j = 1, 2, \dots, r$).

To the end, the first r POD modes $\boldsymbol{\psi}_j$ ($j = 1, 2, \dots, r$), which are the appropriate columns of matrix U , can be calculated from eigenvectors \mathbf{A}_j and the snapshots:

$$\boldsymbol{\psi}_j = \frac{\sum_{m=1}^M A_{m,j} \mathbf{u}'_m}{\|\sum_{m=1}^M A_{m,j} \mathbf{u}'_m\|}, \quad j = 1, 2, \dots, r, \quad (7)$$

where $A_{m,j}$ is an m th component of the eigenvector \mathbf{A}_j corresponding to the eigenvalue ξ_j , and $\|\cdot\|$ is the Euclidean norm.

The fluctuating velocity snapshots can be represented as the linear combination of the POD modes $\boldsymbol{\psi}_j$ with their corresponding POD coefficients \mathbf{a}_j . By projecting the velocity snapshot onto the POD modes, one can obtain the POD coefficients \mathbf{a}_j :

$$\mathbf{a}_j = \boldsymbol{\Psi}^T \mathbf{u}'_j, \quad j = 1, 2, \dots, r, \quad (8)$$

where $\boldsymbol{\Psi} = [\boldsymbol{\psi}_1, \boldsymbol{\psi}_2, \dots, \boldsymbol{\psi}_r]$. Then, the expansion of the fluctuating part of a snapshot j is given by

$$\mathbf{u}'_j = \sum_{p=1}^r a_{p,j} \boldsymbol{\psi}_p = \boldsymbol{\Psi} \mathbf{a}_j, \quad j = 1, 2, \dots, r, \quad (9)$$

where $a_{p,j}$ is the p th component of the coefficient \mathbf{a}_j .

Finally, to obtain the low-ranking approximation in subspace $\mathbb{R}^k \subset \mathbb{R}^M : k \ll M$ with the POD, it is enough to retain the first k singular elements in matrix Σ while all the other elements setting equal to zero. Then, the previous analysis starting from (7) can be formally repeated with the replacement of r by k . As noted above, this approximation is the optimal in the Euclidean norm.

From (6) it is clear that the squared POD coefficients reflect the kinetic energy contained in the corresponding POD modes (see also (Fukunaga, 1990)). Therefore, the POD modes are ranked with respect to their energy.

Thus, the most significant large-scale flow structures, if the flow has, appear in the first POD modes which are the most energetic. It hence provides a possibility to reconstruct the flow only with the first few POD modes while enable to capture the dominant flow features. For more details on the POD, the researchers are encouraged to read (Holmes et al., 2012).

3. Dynamic mode decomposition

The DMD is applied according to the method mentioned in (Rowley et al., 2009), and it is summarised below. Consider a discrete-time flow dynamics system $\mathbf{u}_{j+1} = \mathbf{f}(\mathbf{u}_j)$ where map \mathbf{f} advances the velocity field from time step j to the next. Such a system can appear, for example, after approximations of the Navier-Stokes equations. The main objective of this study is to analyse the flow dynamics only with the use of available flow data or snapshots. To tackle this problem, the Koopman operator is further used.

The Koopman operator U is a linear infinite-dimensional operator $Ug(\mathbf{u}) = g(\mathbf{f}(\mathbf{u}))$, where g is a scalar-valued observable associating a scalar with a flow field. To analyse the flow dynamics, the eigenfunctions and appropriate eigenvalues of the operator U can be determined: $U\varphi_j(\mathbf{u}) = \lambda_j \varphi_j(\mathbf{u})$, $j = 0, 1, \dots$

According to (Rowley et al., 2009), we can introduce a vector-valued observable \mathbf{g} . It can be, for example, a set of the velocity vectors measured at various points in the flow. Next, we

assume that \mathbf{g} lies within the span of the eigenfunctions of the Koopman operator:

$$\mathbf{g}(u) = \sum_{j=1}^{\infty} \varphi_j(\mathbf{u}) \boldsymbol{\phi}_j. \quad (10)$$

If this is not the case, we consider a projection of \mathbf{g} onto the span.

Then, from the definition of the Koopman operator, it follows that

$$\mathbf{g}(\mathbf{u}_k) = \sum_{j=1}^{\infty} \lambda_j^k \varphi_j(\mathbf{u}_0) \boldsymbol{\phi}_j, \quad (11)$$

where $\boldsymbol{\phi}_j$ are the Koopman modes of the map f , corresponding to the observable \mathbf{g} . It is worth noting that if \mathbf{u} is periodic in time, then the Koopman modes reduce to a temporal Fourier transform.

Thus, the flow dynamics can be decomposed into the Koopman modes. In addition, the Koopman eigenvalues characterise the temporal behaviour of the corresponding Koopman modes. It is to be noted that, in contrast to POD, the basis functions represented by the Koopman modes are not necessarily orthogonal. The real part of λ_j determines the growth rate whilst its imaginary part identifies the frequency.

Computing exactly the Koopman modes is excessively expensive. However, they can be approximately calculated with the use of the Arnoldi algorithm as proposed by Schmid ([Schmid, 2010](#)).

Next, consider the sequence of m snapshots taken with an interval Δt in time $\mathbf{V}_0^{m-1} = [\mathbf{u}_0, \mathbf{u}_1, \dots, \mathbf{u}_{m-1}]$, where vector $\mathbf{u}_j \in \mathbb{R}^{3N}$ stands for a j th flow field. Assume that there is a linear operator \mathbf{A} to step forward in time the snapshots: $\mathbf{u}_{j+1} = \mathbf{A}\mathbf{u}_j$. It is easy to see that the eigenvalues of operator \mathbf{A} are also the eigenvalues of the Koopman operator. In addition, the eigenvectors of \mathbf{A} coincide with the Koopman modes if the observable $\mathbf{g}(\mathbf{u}) = \mathbf{u}$.

If the time series is sufficiently long, the last snapshot \mathbf{u}_m can be approximated as a linear combination of its previous $m - 1$ snapshots. Then, the following relation is valid

$$\mathbf{V}_1^m = \mathbf{A}\mathbf{V}_0^{m-1} = \mathbf{V}_0^{m-1}\mathbf{M} + \mathbf{r}\mathbf{e}_m^T, \quad (12)$$

where \mathbf{M} is a matrix of companion type, $\mathbf{e}_m \in \mathbb{R}^m$ is the m th unit vector and \mathbf{r} is a residual that is not equal to zero if the linear dependence is not satisfied. The minimal residual in the Euclidean norm presumes the vector \mathbf{r} is orthogonal to $\text{span}[\mathbf{u}_0, \mathbf{u}_1, \dots, \mathbf{u}_{m-1}]$, according to the Ritz method.

In general, matrix \mathbf{M} satisfying (12) is not unique. One solution for \mathbf{M} is

$$\mathbf{M} = (\mathbf{V}_0^{m-1})^+ \mathbf{V}_1^m. \quad (13)$$

where $(\mathbf{V}_0^{m-1})^+$ is the Moore-Penrose pseudoinverse matrix of \mathbf{V}_0^{m-1} . This solution is unique if matrix \mathbf{V}_0^{m-1} has linear independent columns.

Note that the operator \mathbf{A} remains unknown. In fact, matrix \mathbf{M} represents the projection of the operator \mathbf{A} onto a Krylov space given by snapshots:

$$\text{span}[\mathbf{u}_0, \mathbf{u}_1, \dots, \mathbf{u}_{m-1}] = \text{span}[\mathbf{u}_0, \mathbf{A}\mathbf{u}_0, \dots, \mathbf{A}^{m-1}\mathbf{u}_0]. \quad (14)$$

It turns out that the eigenvalues $\tilde{\lambda}_j$ of matrix \mathbf{M} almost coincide with some of the eigenvalues of the operator \mathbf{A} . Thus, the DMD eigenvalues $\tilde{\lambda}_j$ of matrix \mathbf{M} approximate the eigenvalues of the

Koopman operator. The eigenvalues $\tilde{\lambda}_j$ are also called the empirical Ritz values. Next, one can
¹⁴⁵ introduce $\mu = \ln(\tilde{\lambda})/\Delta t = \sigma + i\omega$. Then, σ and ω represent the growth rate and the frequency
of the mode, respectively.

Consider $\tilde{\Phi} = [\tilde{\phi}_0, \tilde{\phi}_1, \dots, \tilde{\phi}_{m-1}] = \mathbf{V}_0^{m-1} \mathbf{T}$, where the columns of \mathbf{T} are the eigenvectors of
 \mathbf{M} . The vectors $\tilde{\phi}_j$ are the approximation of the appropriate Koopman modes scaled by $\varphi_j(\mathbf{u}_0)\phi_j$.
Thus,

$$\mathbf{u}_k \approx \sum_{j=0}^{m-1} \tilde{\lambda}_j^k \tilde{\phi}_j = \sum_{j=0}^{m-1} \tilde{\lambda}_j^k b_j \bar{\phi}_j, \quad k = 0, 1, \dots, m, \quad (15)$$

where $b_j = \|\tilde{\phi}_j\|_2$ is a DMD mode amplitude, and $\bar{\phi}_j = \tilde{\phi}_j / \|\tilde{\phi}_j\|_2$ is a normalized DMD mode.

It is to be noted that this expansion is exact if $k = 0, 1, \dots, m-1$. In contrast to the
original Arnoldi algorithm, the columns of the companion matrix \mathbf{M} (and hence the modes) are
¹⁵⁰ not necessary orthogonal. This is a payment for not using the explicit operator \mathbf{A} that is unknown.

The algorithm described above is relatively simple but may be ill-conditioned for large values
of m . A robust algorithm, which is based on SVD decomposition of \mathbf{V}_0^{m-1} , can be found in
(Schmid, 2010). The ill-posedness of the problem to identify matrix \mathbf{M} can be overcome via its
reduction to a variation problem (Jovanović et al., 2014). Then, matrix \mathbf{M} can be determined by

$$\min \|\mathbf{V}_1^m - \mathbf{V}_0^{m-1} \mathbf{M}\|_F,$$

where index F means the Frobenius norm: $\|Q\|_F^2 = \text{trace}(Q^T Q) = \text{trace}(QQ^T)$.

To reconstruct the flow, coefficients $\mathbf{b} = [b_0, b_1, \dots, b_r]$ are needed:

$$\min_{\mathbf{b}} J(\mathbf{b}) = \|\mathbf{V}_0^{m-1} - \Phi_r D_b V_{and}\|_F, \quad (16)$$

where $r = \text{rank}(\mathbf{V}_0^{m-1}) \leq m$, $\Phi_r = [\bar{\phi}_0, \bar{\phi}_1, \dots, \bar{\phi}_r]$, D_b is the diagonal matrix with respect
to \mathbf{b} having dimension $[r \times r]$, and V_{and} is the Vandermonde matrix with respect to $\tilde{\lambda}$ having
dimension $[r \times m]$.

This approach can be modified via the sparsity-promoting DMD (DMDSP) method (Jovanović et al., 2014) in which the coefficients \mathbf{b} are found from a variation problem:

$$\min_{\mathbf{b}} J(\mathbf{b}) + \gamma \|\mathbf{b}\|_1, \quad (17)$$

¹⁵⁵ where $\gamma > 0$.

This approach corresponds to Tikhonov's regularization. In the algorithm a solution with a
large norm in L_1 is penalized to make the basis sparser. DMDSP selects a subset of standard
DMD modes and optimizes the amplitude of the selected modes. In this way, the highly damped
modes are likely to be omitted.

The optimized DMD (DMDO) method proposed by (Chen et al., 2012) allows the number
of modes to be significantly reduced. In the approach the modes and eigenvalues are determined
from some approximation requirements while the total number of modes is limited. More formally,
introduce an arbitrary $p > m$. Then, consider an approximation a set of p snapshots:

$$\mathbf{u}_k = \sum_{j=0}^{m-1} \mu_j^k \mathbf{v}_j + \mathbf{r}_k, \quad k = 0, 1, \dots, p-1. \quad (18)$$

The sets $\{\mathbf{v}_j\}_{j=0}^{m-1}$ and $\{\mu_j\}_{j=0}^{m-1}$ are determined via minimization of the total residual:

$$\min \|\Gamma\|_F = \sum_0^{p-1} \|\mathbf{r}_k\|_2^2. \quad (19)$$

¹⁶⁰ Thus, the observables can be expanded with a finite number of DMD modes instead of an infinite number of Koopman modes in (11). From the practical point of view, only a small subset of DMD modes should be selected according to a specific ranking adopted.

Further, we consider four DMD methods for extracting the DMD modes. The first method (denoted as DMDS1) is based on ranking according to the amplitudes of the standard DMD modes (DMDS) in (16). The DMD modes are often ranked by their amplitudes b_j , which represent their contributions to the total energy in the flow field (Bagheri, 2010; Rowley et al., 2009). However, highly damped modes make negligibly small contribution regardless their amplitude in a long term. Taking this into account, another ranking method (DMDS2) proposed by Tissot *et al.* (Tissot et al., 2014) represents the averaged amplitude of the mode over a period of time $[0, T]$ as follows:

$$\frac{1}{T} \int_0^T \|b_j \lambda_j^{t/\Delta t}\|^2 dt = b_j \frac{e^{2\sigma_j T} - 1}{2\sigma_j T}. \quad (20)$$

¹⁶⁵ In addition, we consider the DMDSP (17) and DMDO approaches. The ranking in the DMDO method is based on the amplitudes $\|\mathbf{v}_j\|$ ($j = 0, 1, \dots, m-1$) from (18) and (19). It is to be noted that each of these approaches represents a linear approximation of the Koopman modes of the original nonlinear problem.

4. Jet in channel crossflow

¹⁷⁰ The DNS simulation is performed by Wu *et al.* (Wu et al., 2017b). The flow configuration and numerical setup are briefly introduced here. Figure 2 shows the fluid domain, in which the jet-exit centre is the origin point, is $[-5.3H, 0H, -3H] \leq [x, y, z] \leq [6.7H, 2H, 3H]$, where x , y and z are the streamwise, wall-normal, and spanwise directions respectively. The Reynolds number based on the bulk channel crossflow velocity $\langle u_c \rangle$, the half channel height H and the kinetic viscosity ν is 3333. The jet-to-crossflow velocity ratio $R = \langle u_j \rangle / \langle u_c \rangle$ is set at 1/6, where $\langle u_j \rangle$ is the bulk jet velocity. The diameter of jet-exit equals the total channel height $2H$. No-slip wall boundary conditions are applied to the top and bottom fluid domain. Periodic boundary conditions are applied to the spanwise planes. A classic laminar parabolic profile is used as the jet inlet profile similar to several previous numerical studies (Salewski et al., 2008; Bagheri et al., 2009; Muldoon and Acharya, 2010; Grout et al., 2011; Ilak et al., 2012). A simple convective outflow boundary condition (Ol'shanskii and Staroverov, 2000) is imposed on the outlet section $(x = X_{\max} = 6.7H)$.

¹⁷⁵ The laminar crossflow is considered here. The parabolic laminar profile is applied as a Dirichlet boundary condition at the crossflow inflow plane ($x = X_{\min} = -5.3H$). The time step of this case is fixed at $1 \times 10^{-4} H / \langle u_c \rangle$, and the snapshots are stored for every 1000 time steps, which results the snapshots are spaced equally in the time of $\Delta t = 0.1H / \langle u_c \rangle$. The snapshots are only stored after the flow fields have become fully developed.

¹⁸⁰ The domain is discretised with $257 \times 193 \times 256$ nodes in the x , y and z directions, respectively. The nodes are equally spaced in the x and z directions but with refinement near the wall

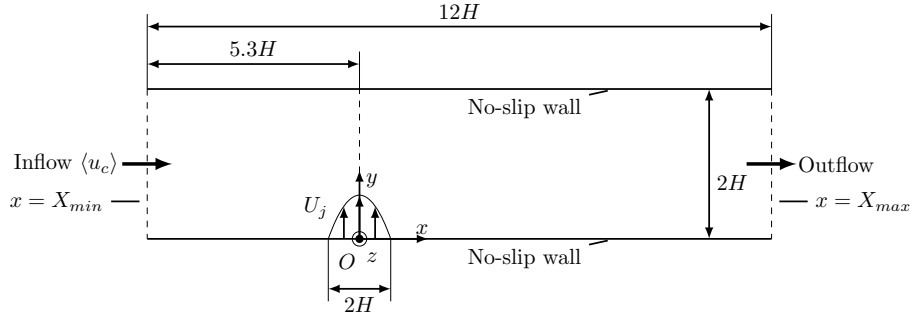


Figure 2: Schematic view of the flow configuration of a jet in channel flow in DNS. The centre of jet-exit is the origin point. The figure is not drawn to scale.

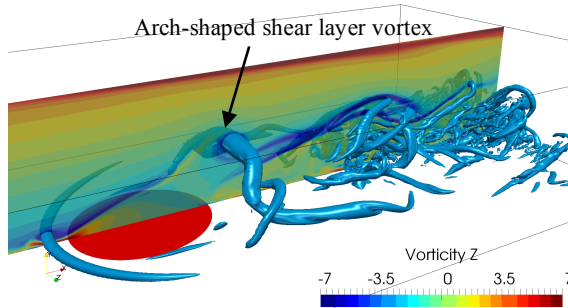


Figure 3: Instantaneous spanwise vorticity on the symmetry plane and the iso-surface of $Q = 7$ in the laminar case. The red circle indicates the jet-exit, and the box outline is the simulation domain.

in the y directions. The DNS simulation is performed with the open source DNS code Incompact3d that is quite accurate and well enough tested (Laizet and Lamballais, 2009; Laizet and Li, 2011). Over 40 publications present numerical methods and validations of this code (cf. <http://www.incompact3d.com/>). Here the sixth-order central compact finite scheme is applied to the velocity field located on a collocated grid. The continuity condition is ensured at the end of every time step by solving the pressure Poisson equation on a staggered grid with the spectral method. The second-order Adams-Bashforth scheme is used for the time-advancement. Further details on the present application including grid resolution study and a more classic Reynolds averaged analysis regarding the mean and second moment velocity and temperature fields can be found in (Wu et al., 2017b).

Besides the time-averaged structures described in Section 1, the unsteadiness of the shear layers is seen in the instantaneous profiles from figure 3. The arch-shaped shear layer vortices are convected downstream along the shear layer with its legs surrounded the jet fluid. They are caused by the jet velocity gradient and the entrainment effect of jet fluid. In addition, the instantaneous laminar profile is found symmetrical about the x -axis and periodic in time.

4.1. Sensitivity analysis

The results of POD/DMD largely depend on the time step of the snapshots Δt and the number of snapshots N_s (equivalent to total time span if Δt is fixed) used in the POD/DMD analysis.

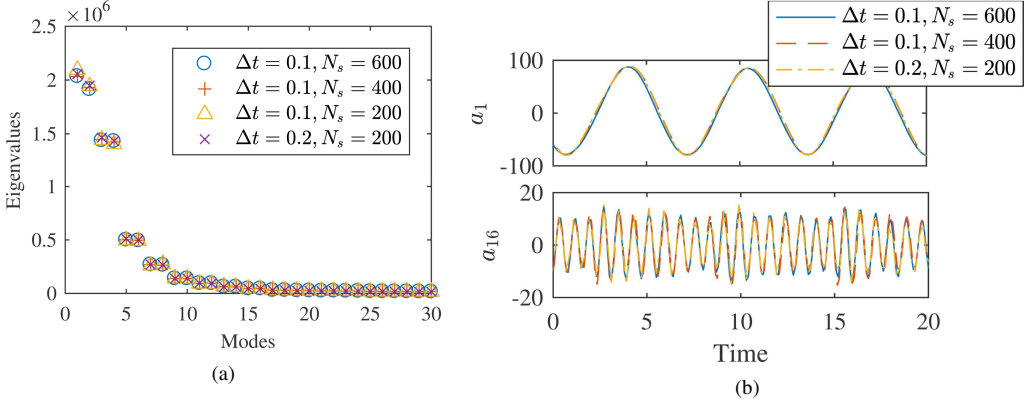


Figure 4: POD sensitivity test: (a) POD eigenvalues and (b) POD coefficients from different datasets. Δt is normalised by $H/\langle u_c \rangle$.

Therefore, in order to extract physically relevant flow structures from POD/DMD analysis, one has to verify if the results are independent of both parameters Δt and N_s .

The sensitivity of POD can be immediately verified by comparing the eigenvalues and eigenvectors from different datasets. Figure 4(a) shows the eigenvalues of each POD mode from four different datasets. The first three datasets have the same sampling frequency Δt but a different number of snapshots N_s , therefore their time spans are different. It is shown that the POD eigenvalues of the three datasets are close to each other: further examination shows that the maximal differences of the first 30 POD eigenvalues are less than 1% between the three datasets. It should be reminded that the 30th POD eigenvalue contains only 0.58% energy of the first one, and is (usually) out of interest in the POD analysis. Therefore, one can conclude that the time span of $40H/\langle u_c \rangle$ (second dataset) is enough for obtaining accurate POD eigenvalues. The fourth dataset has a double time step but the same time span as the second dataset. The POD eigenvalues of these two datasets are also close to each other.

The eigenvector structures can be examined by comparing the POD coefficients. This is obvious as the POD coefficients are the results of projecting the velocity snapshots onto the POD modes (see (8)). Only the coefficients of the first three datasets that have close eigenvalues are checked. Figure 4(b) shows the quasi-periodic fluctuations of POD modes 1-16 are well captured from these datasets (a_2 to a_{15} are not shown here for simplicity). Beyond mode 16, the results begin to diverge. The 17th mode contains less than 1.5% energy of the most energetic one. Since the analysis of POD modes is entirely based on the energy, it is acceptable that at least the first 16 POD modes converge. Thus, we conclude that $\Delta t = 0.1H/\langle u_c \rangle$ and $N_s = 400$ are adequate to resolve the POD modes in the current laminar flow configuration.

The sensitivity analysis of DMD is more complicated. Similar to the POD, DMD results are also affected by the Δt and time span (or N_s). DMD separates the modes by frequency. Similar to the temporal Fourier transform, the highest frequency that DMD can resolve is limited by $\frac{1}{2\Delta t}$ according to the Nyquist sampling theorem. On the other hand, the lowest frequency we can resolve with DMD is constrained by the time span of datasets. Next, we study the influence of the parameters Δt and time span.

It is reasonable to assume that a fully-developed flow evolves towards an attractor (steady state): the DMD modes should lay near the unit circle as the Koopman operator is unitary

([Bagheri, 2010](#)). Thus, those physically relevant modes, which are steady, should keep the same if the DMD is performed on different datasets obtained from the same flow.

With this idea, we carried out DMD over the four datasets, with different Δt or time span. Figure 5 only shows the modes with a growth/damping rate $|\sigma| < 10^{-2}$. From (20), it is easy to show that a mode with growth/damping rates of 10^{-2} is equivalent to averaging 70% of the original energy over the time span $40H/\langle u_c \rangle$. It is shown from figure 5(a) that these modes with small growth/damping rates consistently appear from the DMD of the four datasets. Further examination shows all the coinciding DMD modes from four datasets all lay on the unit circle. On the other hands, the modes with larger growth/damping rates do not consistently appear in different datasets. These modes are not physical meaningful, and they are considered as spurious by Semeraro *et al.* ([Semeraro et al., 2012](#)). Figure 5(b) shows the amplitudes of the selected DMD modes. As can be seen, the coinciding modes have similar amplitudes. This is obvious as these peaks are directly linked with the same instability mechanisms or the physically relevant motions from the same flow. However, three main questions remain open: (1) what happens if Δt decreases, (2) what happens if the time span increases, and (3) why the appropriate amplitudes are not exactly the same in different datasets. Next, the answers to these questions are discussed.

If the sampling frequency Δt decreases, DMD can resolve oscillations at higher frequencies. Nevertheless, figure 5(b) shows the amplitude decays fast as the frequency increases in the current flow configuration: in fact, the amplitudes decay exponentially according to the frequency $b_j \propto \exp(-|St|)$. Thus, even though DMD can resolve motions at a higher frequency with a smaller Δt , those modes will not be the most dominant modes. Therefore, $\Delta t = 0.1H/\langle u_c \rangle$ seems adequate in this flow.

If the dataset time window increases, DMD can resolve the motion at lower frequencies. As can be seen in figure 5(b), the modes linked with the instability mechanism or physically relevant motions follow harmonic modes with the lowest frequency corresponding to $St = 0.155$. A linear combination of these harmonic modes excites other modes, similar to what is observed in ([Rowley et al., 2009](#)). Thus, the time span ($40H/\langle u_c \rangle$) is sufficient for this flow.

Finally, the amplitudes are not always the same in different datasets because a higher frequency can be resolved when increasing the number of snapshots as mentioned in ([Muld et al., 2012](#)). Therefore the frequency band of each mode becomes smaller, and the energy of each mode also changes.

Thus, the DMD sensitivity analysis is more difficult than that with the POD. In a turbulent flow with a broad band spectrum, the dominant motions with the lowest and highest frequencies are unknown. Although one can carry out the temporal Fourier transform on the velocity signal at a probe to obtain a preliminary knowledge on the frequency band of the flow, this velocity temporal spectrum is only related to the probe; the global information still retains unknown. Thus, it is problematic to complete a rigid DMD sensitivity analysis. In turn, if the lowest and highest frequencies are large enough, then the DMD is constrained by the computer memory.

At last, as the result of the above sensitivity analysis, 400 snapshots equally spaced in the time by Δt , are used to perform the POD and DMD. Figure 6 shows the percentage of the velocity fluctuation energy in each POD/DMD mode and the cumulative energy, which are summarized in table 1. Firstly, the energy of first two DMDS modes is lower than that in the POD modes (third column in table 1). Secondly, the energy is more evenly distributed in DMD. For example, (1) more modes contain more than 10% of the energy of the first mode in DMDS than that in the POD (fourth column in table 1), and (2) the top 5% of DMDS modes (that is 20 modes) only contain 64% of total energy in DMDS, compared to 89% in the POD (not listed in the table). Thirdly, the POD proves to be preferable regarding the energy content/decay rate across

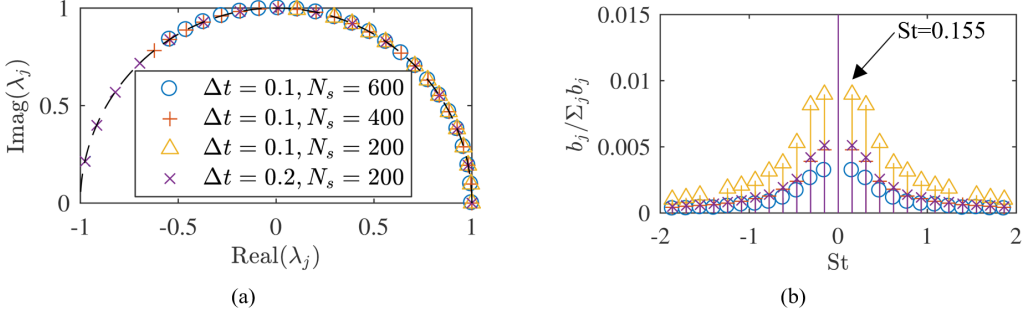


Figure 5: DMD sensitivity test: (a) selected DMD mode dynamics and (b) selected DMD mode amplitudes from different datasets. The selection criteria is the growth/damping rate $|\sigma| < 10^{-2}$. Δt is normalised by $H/\langle u_c \rangle$.

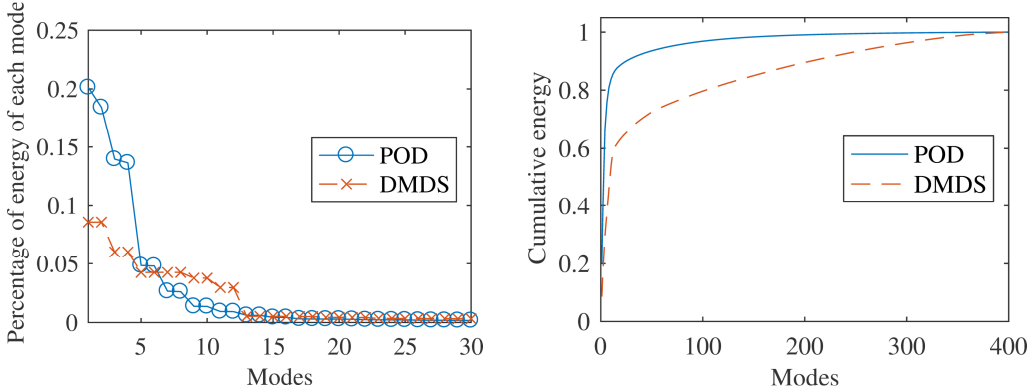


Figure 6: Percentage of the energy of each mode (left) and cumulative energy (right) in the jet in laminar channel crossflow.

the modes, as the DMD series requires much more modes to capture the same amount of energy. To reconstruct 99% of the total kinetic energy, around 49% of the POD modes is needed. This number increases to 90% in the DMD (last column in table 1). This is quite a large number if the researchers want to use the reduced order modelling (Liakopoulos et al., 1997) to reconstruct the flow. The reduced order modelling usually uses an order of magnitude fewer equations to reconstruct the flow with 99% of the total energy.

5. POD modes of JICF

In this section, the fluctuation snapshots are decomposed onto orthogonal bases using POD. The most dominant modes based on the energy are identified. The POD mode eigenvalues represent the kinetic energy of the corresponding modes. The eigenvalues are normalised to represent their relative percentages of energy, which are shown in the POD mode figures. In addition, it is to be noted that, to reconstruct the fluctuating snapshots, the POD modes must be scaled by the time-varying corresponding coefficients as in (9). Thus, the original vector lengths or scalar magnitudes in POD modes have no physical meaning. This is also applied in the DMD mode analysis.

	Energy of first two modes	Number of modes containing more than 10% of energy of the first mode	Number of modes needed to reconstruct 99% of total energy
400 modes	POD 20.1% & 18.4%	8 (2.0%)	194 (49%)
	DMDS 8.6% & 8.6%	12 (3.0%)	358 (90%)

Table 1: Summary of POD and DMDS of the current jet in channel flow case with snapshots equally spaced with $\Delta t = 0.1H/\langle u_c \rangle$. The percentage numbers in bracket are the percentage of total number of modes: for example, 8 out of 400 POD modes in POD contains more than 10% of energy of first modes, that is $8/400 = 2.0\%$

Figure 7 shows the time-variance of POD mode coefficients a_i , which exhibit the phase-shifted sine behaviour. It is obvious that the coefficients of each two POD modes display the same frequency but with the phase shifted by about a quarter of wavelength. Thus, we group POD modes 1 and 2 as the POD pair 1, modes 3 and 4 as the pair 2, modes 5 and 6 as the pair 3, modes 7 and 8 as the pair 4, and so on. In addition, the dominant frequencies of the POD coefficients increase from the POD pair 1 to POD pair 4. This is seen in the spectra or the Lissajous curves of the POD coefficients in figure 8: the coefficients of each two modes have their peaks at the same frequency, and the most energetic frequency of POD pair k is k times the first pair ($St_k = 0.150k$). However, it is also noted from figure 8 that in general one POD mode contains multiple frequencies.

Figure 9 shows the streamwise velocity signals in the flow at two probes from the stored snapshot series, which is also used for POD and DMD post-processing. The first probe, corresponding to signal u_1 , is located in one of the legs of the horseshoe vortex at $[x/H, y/H, z/H] = [1.22, 0.10, 2.32]$. The second probe, signal u_2 , is located at $[x/H, y/H, z/H] = [0.38, 0.58, 0]$ in the shear layer. Oscillatory behaviour of the signals is obvious in this case. The normalised frequency contents $\hat{u}_1(St)$ and $\hat{u}_2(St)$ of $u_1(t)$ and $u_2(t)$ respectively, are presented in figure 10. Both signals show low-frequency features, but u_2 also contains an information with a higher frequency.

The sum of all the POD modes results in the full flow field. POD mode 1/2 has the dominant frequency of $St = 0.15$ which is close to that of the u_1 signal. As the u_1 signal is located in one of the legs of the horseshoe vortex, POD mode 1/2 shows the features of the horseshoe vortex. Figure 11(a-b) shows the first two POD modes (mode 1 and 2). The profiles on $y/H = 0.60$ plane show great symmetry properties as this laminar flow is symmetric. The first POD mode captures vortices at the front edge of jet-exit on the symmetry plane ($z/H = 0$). The upstream vortices are recognised as the horseshoe vortex in the iso-surface of Q-criterion ($Q = 5 \times 10^{-5}$) plot (see figure 12(a)). An upward effect is seen downstream before $x/H = 3$ and is followed by a strong downwash effect. This may relate to the re-attachment of the jet fluid. Mode 2 shows an almost identical structure to the mode 1, only with a shift of $\sim 1.5H$ in the downstream direction. The re-attachment point is moving backward and forward periodically in the current flow, similarly to that in a backward-facing step, and the POD modes 1 and 2 seem to describe two stages of the flow fluctuating motion. This is confirmed as the corresponding coefficients a_1 and a_2 change as phase-shifted sine waves in time, so that when the first two modes combined with their coefficients, they could capture the flow convection. Further comparisons showed that the modes 3 and 4, modes 5 and 6, etc. have almost identical spatial patterns with a shift in space,

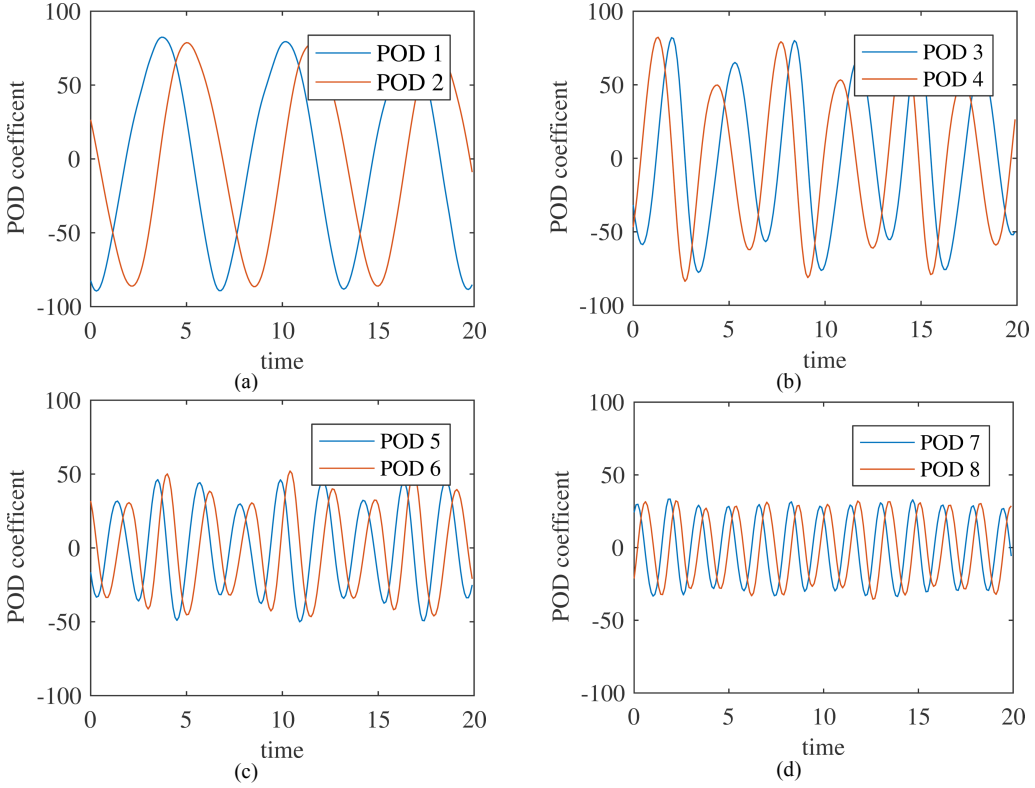


Figure 7: The variation of POD coefficients a_i with time in the parabolic laminar crossflow case.

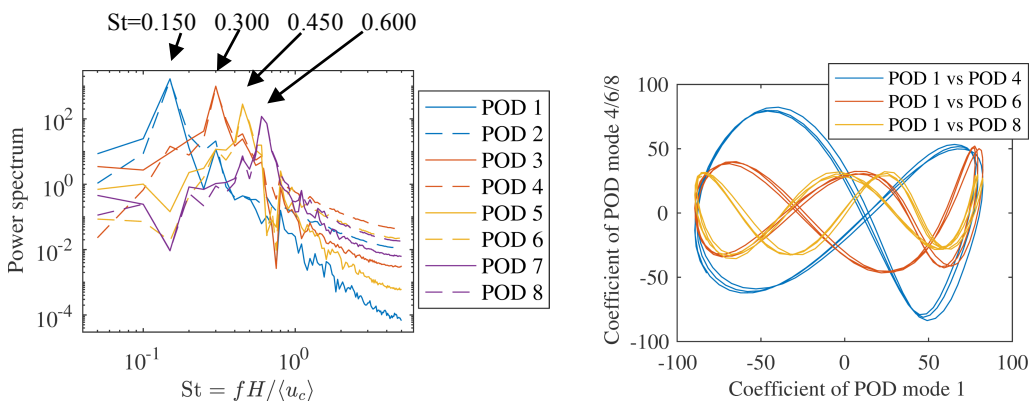


Figure 8: Spectra (left) and the Lissajous curves (right) of POD coefficients a_i .

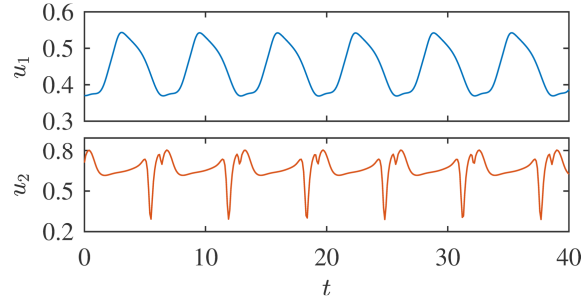


Figure 9: Streamwise velocity signals at two probes. The u_1 signal (blue) is recorded in one of the legs of the horseshoe vortex ($[x/H, y/H, z/H] = [1.22, 0.10, 2.32]$), while the u_2 signal (orange) is recorded in the shear layer region ($[x/H, y/H, z/H] = [0.38, 0.58, 0]$).

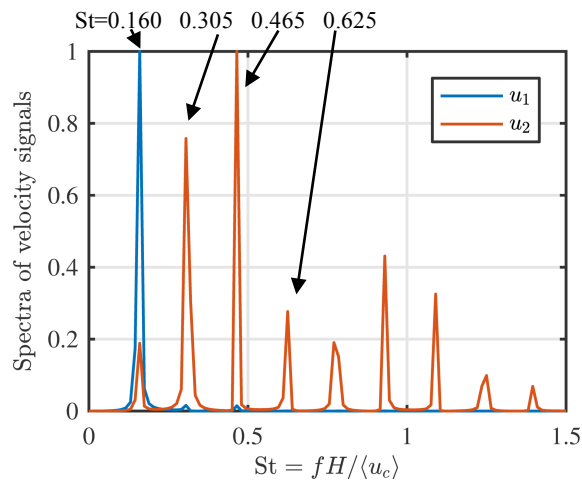


Figure 10: The frequency representations of the velocity signals (colour). The spectra are normalised by their own peaks respectively.

similar to that in mode 1-2 and what observed by Meyer *et al.* (Meyer et al., 2007).

The u_2 signal at the shear layer region has dominant frequencies at $St = 0.305, 0.465$ and 0.625 . These frequencies are corresponding to POD modes $3/4, 5/6$ and $7/8$ in figure 8(b-d).
335 Thus, these POD modes are linked to the shear layer vortices. Figure 11(c-e) show POD modes $3/4, 5/6$ and $7/8$ respectively. In mode $3/4$ (figure 11(c)), the horseshoe vortex is still as clearly seen as in mode $1/2$. Some structures in the downstream of shear layer become recognisable in the vector plot. On the $y/H = 0.60$ plane, vortex pairs placed along two sides of the symmetry axis are seen. These vortex pairs are the footprint of the arch-shaped shear layer vortices (see
340 figure 3(a)). The horseshoe vortex is the most energetic. Therefore, from mode $3/4$ (figure 11(c)) to mode $7/8$ (figure 11(e)), the horseshoe vortex gradually disappears while the shear layer vortices become more evident.

Figure 12(b) shows an example of the Q-criterion of these POD modes. The shear layer vortices are identified as that in the POD modes of a jet in boundary layer crossflow with higher velocity ratio $R = 3.3$ (Meyer et al., 2007). As noticed in figure 8, the dominant frequency of the POD modes increases as the mode index increases, which corresponds to the decrease of the wavelength. This is reflected in the space structures of POD modes: in figure 11, the wavelengths of the shear layer vortices become shorter as the POD mode indexes increase. Along the curve of interaction between the inlet free-stream flow and jet the Kelvin-Helmholtz instability
345 is developed. Behind this curve a region with the vortical instability occurs. Modes 5-8 capture the vortices caused by both the Kelvin-Helmholtz and vortical instabilities. In turn, modes 3-4 capture only the structure of the vortical instability since such vortices contain greater energy.
350

6. DMD modes of JICF and their ranking

6.1. DMD analysis

The flow is derived from a non-linear dynamical system (the Navier-Stokes equations). It is shown that the Koopman modes or the DMD modes extract the global oscillatory behaviour in one go. In the POD analysis, it is found that the POD pairs are phase-shifted to represent the periodic oscillations. Bidan & Nikitopoulos (Bidan and Nikitopoulos, 2013b) found that the convective motions are captured by the real and imaginary parts of the complex DMD modes.
355 Thus, only the real parts of the DMD modes are presented here.

As discussed in the sensitivity study, we found those DMD modes which consistently appear in different datasets directly linked with the physically relevant modes or the instability mechanism. We refer to these DMD modes as the converged ones. Therefore, only the converged DMD modes are analysed. The converged DMD modes are ranked by their amplitudes shown in figure 5. So the converged DMD mode 0 is the one with $St = 0$, the converged DMD mode 1 is the mode with $St = 0.155$, and so on.
360

Figure 13 shows the first three converged DMD modes. Similar to the POD, the converged DMD modes that have the same dominant frequency as u_1 signal should present horseshoe vortex structures, while those modes that have the same frequency as u_2 signal should show the oscillations along the shear layer. Converged DMD mode 1 has the frequency of $St = 0.155$ (figure 13(a)) which is also the dominant frequency of the u_1 signal. As the u_1 signal is located in one of the legs of the horseshoe vortex, DMD mode 1 shows the features of the horseshoe vortex. Figure 13(a) shows the converged DMD mode 1. The instability of the horseshoe vortex at the upstream edge of jet-exit is seen in this mode, as well as a downwash effect in the far downstream. Mezić
370

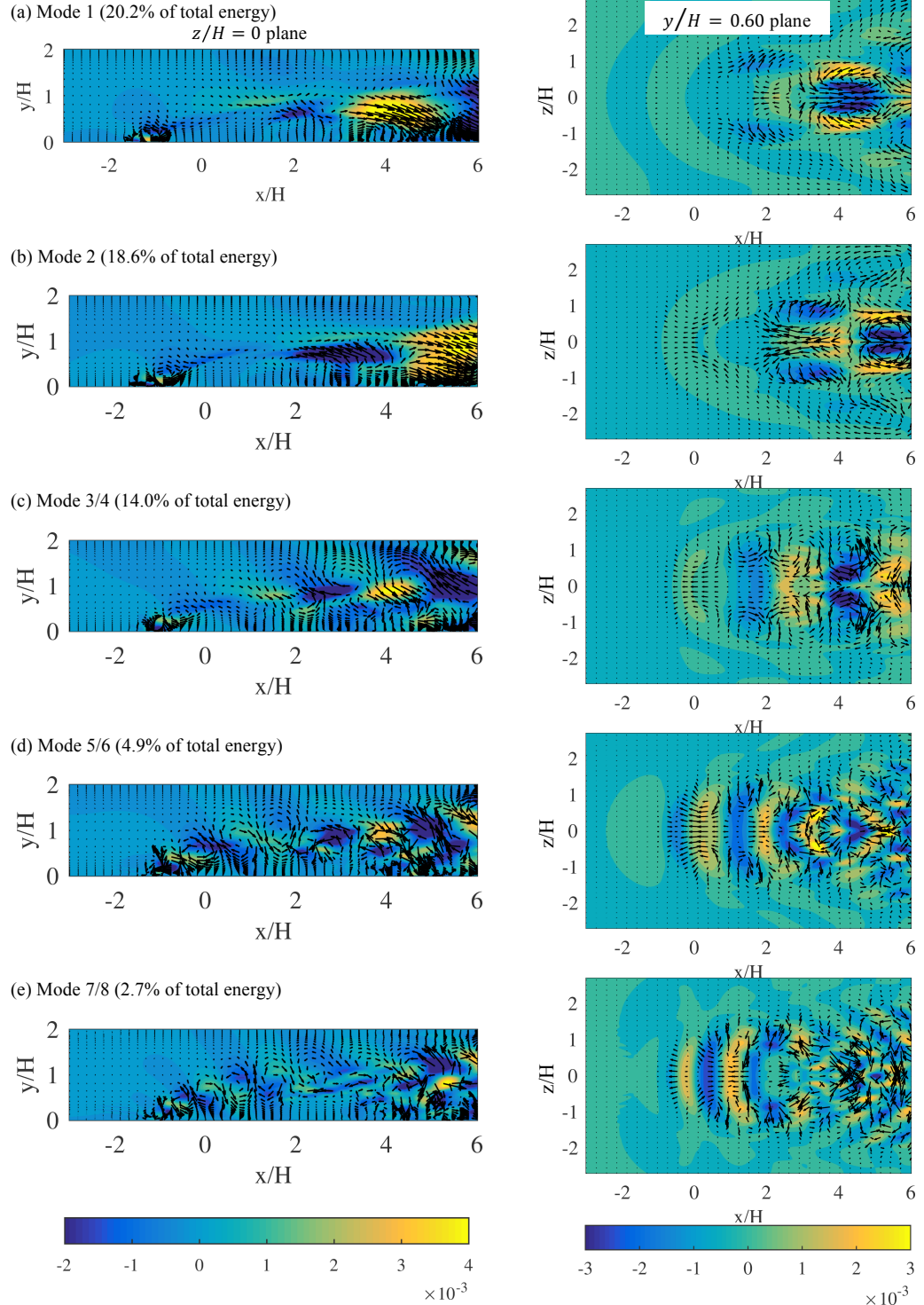


Figure 11: Top POD modes in the parabolic laminar crossflow case: (a-e) modes 1, 2, 3/4, 5/6 and 7/8. The left column shows the in-plane velocity vector with u contour on the symmetry plane ($z/H = 0$). The right column shows the in-plane velocity vector with v contour on $y/H = 0.60$ plane.

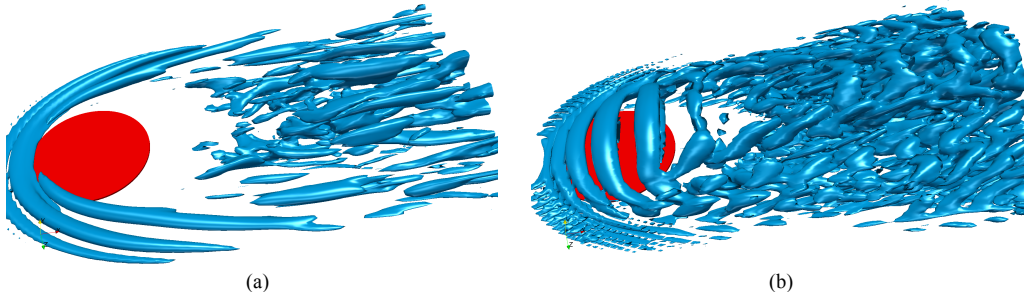


Figure 12: The iso-surface of Q-criterion ($Q = 5 \times 10^{-5}$) of POD (a) mode 1 and (b) mode 7. The red circle indicate the jet-exit.

375 concluded in his review paper (Mezić, 2013) that the Koopman analysis can unravel the connections of flow structures in different parts of the flow domain. In the present mode, it unravels the interaction of the horseshoe vortex in the upstream of jet-exit and downstream in far wake.

380 The dominant frequencies of u_2 signal corresponds to converged DMD modes 2/3 in figure 13(b-c). Thus, these DMD modes are linked to the shear layer vortices. Vortex structures along the shear layer are seen on the symmetry plane; the shear layer vortices firstly form at the windward side of jet-exit, and then gradually break down into small eddies owing to viscous dissipation. The arch-shaped shear layer vortices are also recognised as the vortex pairs on the $y/H = 0.6$ plane. The converged DMD mode 3 has a higher frequency than mode 2, so it shows a shorter wavelength of the shear layer vortices.

385 In figure 14, the 3-D spatial structures of selected converged DMD modes are presented. Each converged DMD mode is characterised by a single frequency. The frequencies of the converged modes are also shown in figure 14. Compared with the POD coefficient spectra in figure 8, the converged DMD frequency information has a closer agreement with the velocity signal spectra in figure 10 (see table 2 for a summary). The appropriate frequencies can characterize 390 the oscillations of the jet as a whole. All the converged DMD modes are harmonic (cf. figure 5). They represent large-scale time-periodic flow structures and shedding of the vortices in different flow region. A linear combination of these harmonic modes excites other modes, similar to what is observed in (Rowley et al., 2009). As noted in (Iyer and Mahesh, 2016), at low values of R the flow becomes self-excited. The superposition of low frequency modes can result in a 395 quasi-periodic global motion (Rowley et al., 2009). Analysing the observable signals recorded by a probe, we obtain the frequency behaviour at that local point only whereas the DMD analysis identifies the global frequency in the whole domain globally and automatically. Moving the probes to a different location would lead to a different picture whereas the DMD mode spectrum is space invariant. By chance u_1 and u_2 arbitrary locations seem aptly chosen. As can be seen 400 from figure 14, low-frequency modes are able to capture the key features of the horseshoe vortex. In turn, the high-frequency modes represent relatively smaller scale shear layer vortices.

405 In contrast to POD, the converged DMD modes starting from mode 2 capture the Kelvin-Helmholtz instability. Both POD and converged DMD modes are able to represent most flow characteristics in this laminar case. Most energetic POD and converged DMD modes have the same dominant frequencies, so the spatial structures of converged DMD and POD modes are found very similar to each other (cf. figure 12 and figure 14). Both the horseshoe vortex and the shear layer vortices are captured by the first few modes containing most energy. However, these

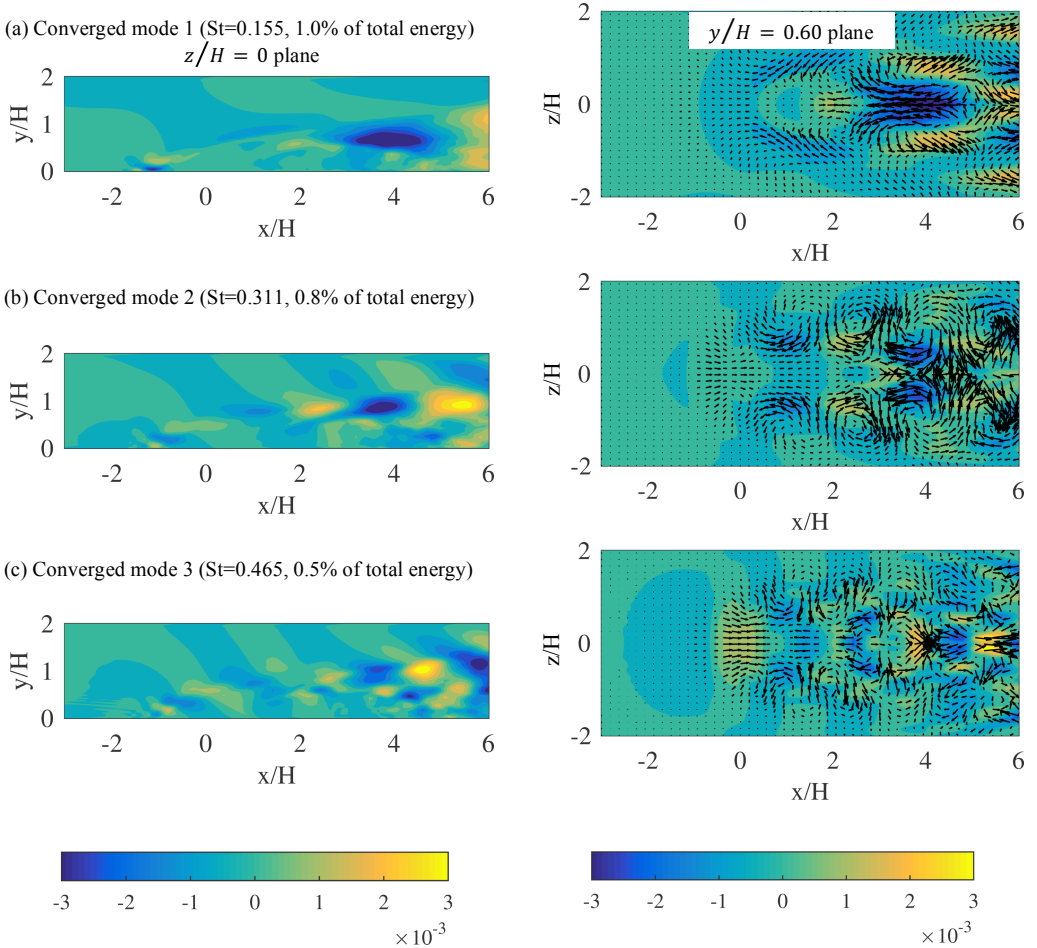


Figure 13: Converged DMD modes 1-3. The left column shows u contour on the symmetry plane ($z/H = 0$). The right column shows the in-plane velocity vector with v contour on $y/H = 0.60$ plane.

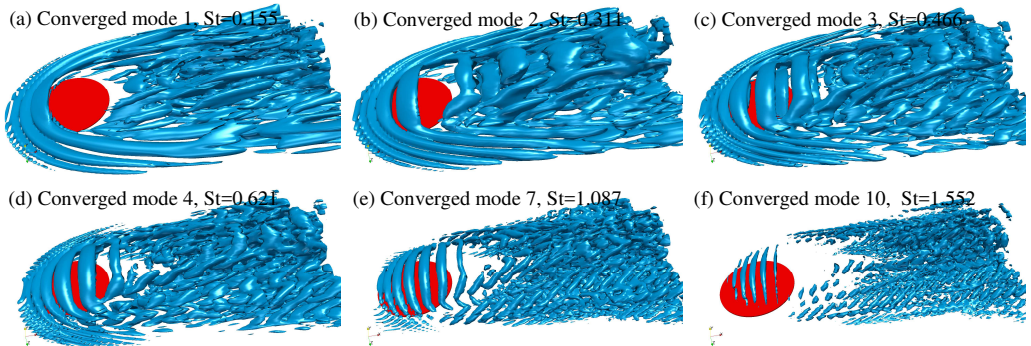


Figure 14: The iso-surface of Q-criterion ($Q = 10^{-2}$) of selected converged DMDS modes. The red circle indicate the jet-exit.

Mode	DNS	POD	DMD
Horseshoe vortex	0.160	0.150	0.155
Shear layer	0.305, 0.465, 0.625	0.300 0.450 0.600	0.311, 0.466, 0.621

Table 2: Comparison of the frequencies obtained from DNS probes (figure 9), POD modes 1-8 (figure 8) and the DMD modes (figure 14)

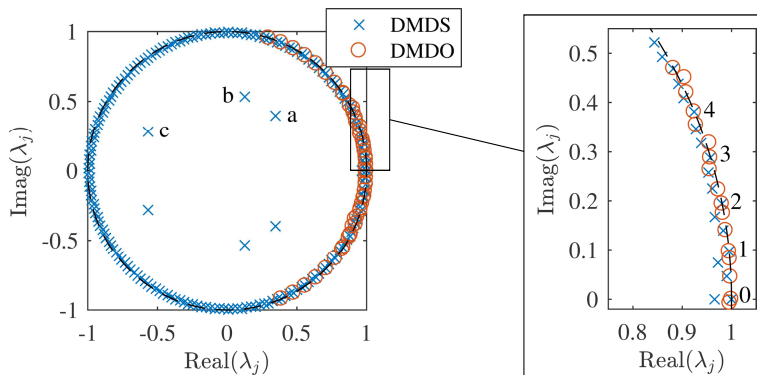


Figure 15: Dynamics of DMD modes in the laminar case. The right figure is the zoom of the left figure. “a”, “b” and “c” are the DMDS modes marked in figure 16. Number 0-4 are the first five DMDO modes which coincide with DMDS modes.

converged DMD modes contain significantly less energy compared with the corresponding POD modes: for example, converged DMD mode 1 only contains 1.0% of total energy (figure 13(a)).

This is because the DMD also generates many other modes with greater energy but these modes are found to be spurious. This issue will be discussed in the next subsection in which we show that the quality of low-order reconstruction can be strongly effected.

6.2. Low-order DMD reconstructions

We then consider a low-dimensional reconstruction based on different DMD approaches (DMDS1, DMDS2, DMDSP and DMDO) introduced in Section 3. 400 DMDS, 400 DMDSP and 50 DMDO modes are generated from 401 snapshots in time interval $t = [0, 40]$.

Figure 15 shows the dynamics of DMDS, DMDSP and DMDO modes. DMDO modes are more stable than DMDS and DMDSP modes, as more DMDO modes lay nearby the unit circle (figure 15). Quantitatively speaking, 27 of 50 DMDO modes, but only 9 of 400 DMDS modes, have damping rates smaller than 10^{-2} . It is also found that some DMDO modes coincide with the DMDS modes. By comparing figures 5 and 15, one can find that all the coinciding DMDO modes are also the converged stable DMDS modes, and they show similar spatial structures (not shown here).

The amplitudes of the DMD modes based on four methods are shown in figure 16. In figure 16, the y -axis represents the relative energy $b_j/\sum_j b_j$ of each DMD modes, while the x -axis corresponds to the frequency $St_j = f_j H / \langle u_c \rangle$ of the modes. Here $f_j = \text{Im}(\log(\lambda_j)) / \Delta t / 2\pi$ and λ_j is the complex eigenvalue of the DMD mode j . As can be seen from figure 16, the DMDO and DMDSP methods reveal the importance of Mode 0 ($St = 0$, “mean” flow), and put more weight

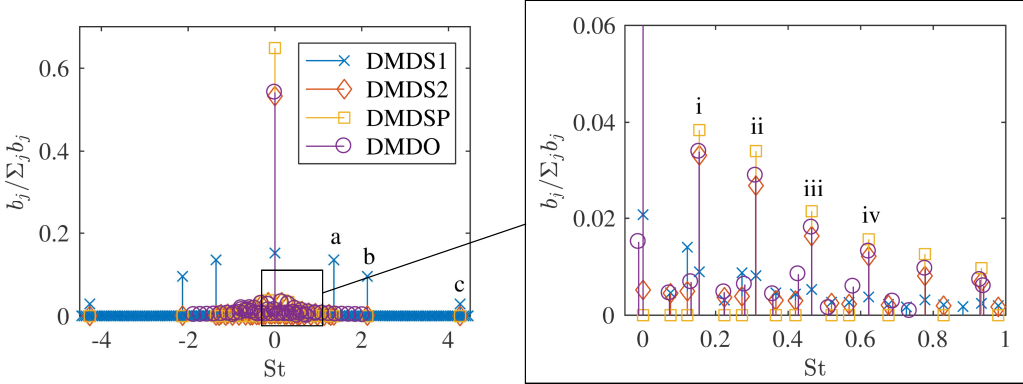


Figure 16: Amplitudes of DMD modes based on four DMD methods.

on the low frequency modes. The DMDS1 does not identify such a priority while DMDS2 displays the importance of the mean flow.

It should be noted that DMDS1 modes marked “a”, “b” and “c” are the modes with the largest energy excluding the mode with zero frequency which corresponds to the “mean” field (see figure 16). However, these three high-amplitude modes have a large damping rate since the Ritz values of these modes are significantly inside the unit circle (see figure 15).

Next, we select a subset of DMD modes, which contain the largest energy among all modes, to approximate the flow. The error of the DMD reconstruction is measured in L^2 :

$$L_m^2 = \|x_m - x_{m,DMD}\|^2 / \|x_m\|^2, \quad (21)$$

where x_m is a snapshot vector from the simulation and $x_{m,DMD}$ is the vector reconstructed from DMD modes. The reconstructions are made with three, five, seven or nine modes at $t = 40H/\langle u_c \rangle$.

As can be seen from table 3, in the DMDS1 the approximation with five modes does not outperform the approximation with three modes. This is because in the DMDS1, mode “a”, “b” and “c” (see figure 16) are selected to reconstruct the flow. However, these modes have strong damping rates. Therefore, the mode contributions vanish with a long time evolution. In turn, the DMDO and the DMDSP demonstrate significant improvements over the DMDS1, while the DMDSP is slightly better than the DMDO if more than three modes are used. However, it is remarkable that the DMDS2 selects the same modes (“i”, “ii”, “iii” and “iv” in figure 16) as the DMDO or DMDSP. The amplitudes in these three methods are very close, although they are slightly higher in the case of the DMDSP. The calculations show that the DMDSP and DMDS2 give almost identical predictions. More precisely, the relative difference between these two reconstructions ($\|x_{m,DMDS2} - x_{m,DMDSP}\|^2 / \|x_{m,DMDSP}\|^2$) is about 0.3% that is negligible.

Next, figures 17 and 18 demonstrate the flow reconstruction from DMD modes at $t = 40H/\langle u_c \rangle$. As already follows from the error analysis, there is no difference between the approximation with three and five DMD modes selected by DMDS1. In addition, the approximations by DMDS2 and DMDSP seem identical.

In figure 17, the counter-rotating vortex pair (CVP) and the horseshoe vortex outside the core wake region are seen in the original snapshot and DMD-based reconstructions. With three modes, all approximations show a stronger CVP and larger horseshoe vortex. With five modes, the approximations with DMDS2, DMDSP and DMDO are nearly identical to each other. However,

	DMDS1	DMDS2	DMDSP	DMDO
3 modes	13.2%	10.0%	10.0%	9.2%
5 modes	13.2%	7.0%	7.0%	7.6%
7 modes	13.2%	5.7%	5.7%	7.4%
9 modes	13.2%	4.9%	4.9%	6.2%

Table 3: Errors in reconstruction error L^2 for different DMD methods with the different number of modes. The DMD modes with largest energy are selected.

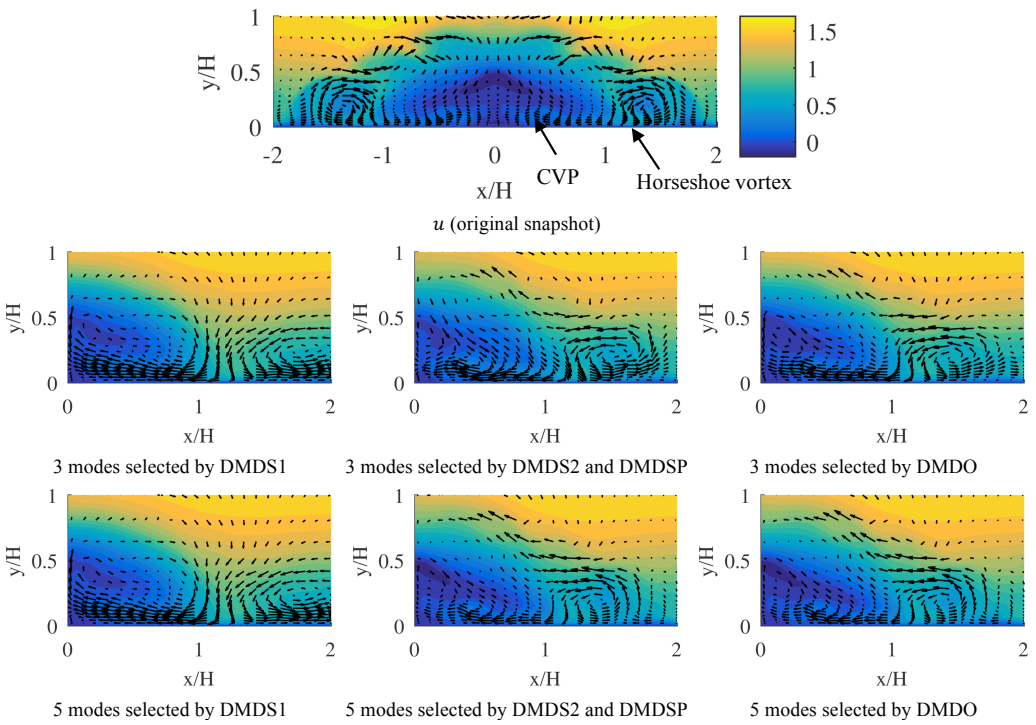


Figure 17: Reconstruction at $x/H = 2.25$ for $t = 40H/\langle u_c \rangle$ with 3/5 modes selected from four DMD approaches in the laminar case. The figures show u contours and in-plane velocity vectors.

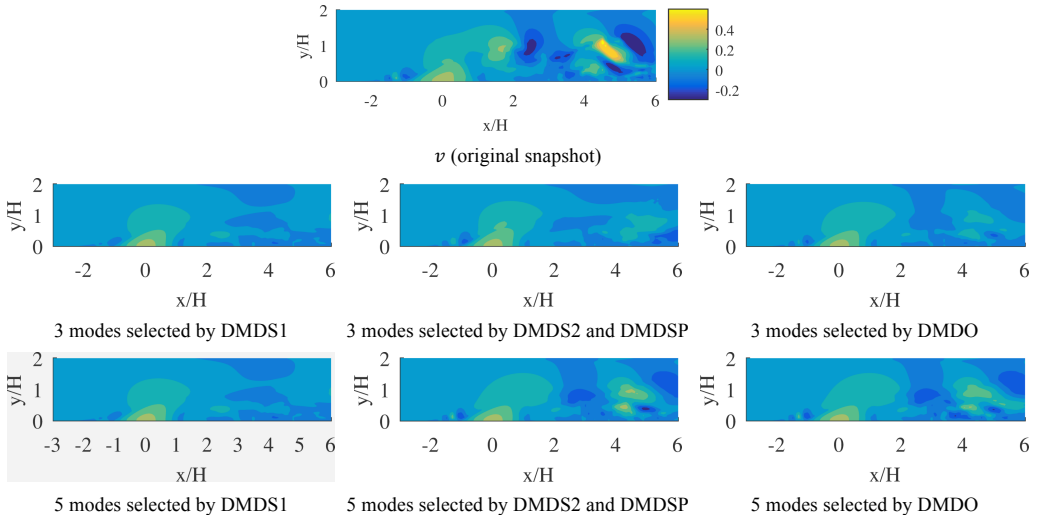


Figure 18: Reconstruction at symmetry plane ($z/H = 0$) for $t = 40H/\langle u_c \rangle$ with 3/5 DMD modes selected from four DMD methods in the laminar case. The figures show v contours.

all of them show a weaker horseshoe vortex in comparison with the original snapshot. This is because these DMD approaches assign too much weight to Mode 0 (“mean” flow). Thus, the low-frequency modes characterising the horseshoe vortex oscillations have less contribution to the flow.

In figure 18, small-scale vortices along the shear layer occur in the original snapshot. All approximations reproduce vortices at the upstream of jet-exit but their scale is much smaller in the wake region. As noted above, high frequency motions are not recognized by the considered DMD approaches as the most dominant modes are characterised by low frequencies. Meanwhile, figure 14 shows that high frequency modes mainly contain small vortices in the wake. Thus, the DMD approximates the wake flow worse in comparison to the upstream region and the downstream near field. To resolve the wake flow better, a local DMD analysis is needed. Overall, in the test case with a laminar crossflow, DMDS2 which is cheaper to compute provides results comparable to those obtained by DMDSP or DMDO.

7. Conclusions

From DNS snapshots of a laminar jet in laminar channel crossflow, DMD and POD modes have been computed and compared. The sensitivity of the POD and DMD modes to the sampling frequency and time span has been studied. The POD sensitivity study is based on comparing the energy and time-varying coefficients of POD modes; the POD eigenvalues varies less than 1% for the first 30 modes, and the POD coefficients of the first 16 modes are collapsed with each other between the four sampling condition we considered. This analysis indicates that the time span is long enough and the sampling frequency is high enough for POD analysis in the current flow. In DMD, the sensitivity study is based on analyzing the dynamics and amplitudes of stable DMD modes. We found that DMD modes with small growth/damping rates consistently appear from the four datasets we considered, while those spurious, not physical meaningful modes do not

480 which have high growth/damping rates. By examining those stable, consistently appear DMD modes, we found as the energy of DMD modes decays exponentially, there is no need to resolve a non-dominant mode which has a higher frequency but significant small energy. On the other hand, as the current flow has a basis flow frequency ($St = 0.155$), increasing dataset time window is also not necessary.

485 As expected, the optimality of the POD has been found in reconstructing the flow. In turn, DMD requires more modes to capture the same amount of energy. The convective motion is captured by POD mode pairs that contain different phases for the same spatial structure. It can also be described by the real and imaginary parts of the complex DMD mode. The results show that the DMD modes automatically reveal the frequency information and corresponding spatial structures in the entire field. In addition, the DMD unravels the interaction of different parts of the flow domain.

490 Four DMD technique have been applied to the problem including the standard approach, optimized DMD and sparsity promoting algorithm. In turn, in the standard DMD the ranking is based on either the mode amplitudes or their averaged over time values. It has been shown that some optimized DMD modes coincide with the standard DMD modes, and these coinciding modes are also the converged stable modes in the DMD sensitivity study. The resulting converged DMD modes illustrate different three-dimensional flow structures and frequencies related to the horseshoe vortex and shear layer as well as the counter-rotating vortex pair. In particular, the horseshoe vortex is related to low-frequency modes, while the shear layer vortices are connected to the high-frequency ones.

500 All four ranking approaches have been applied to a low-dimensional flow reconstruction and compared against each other. It has been shown that the ranking of DMD modes with the use of period-averaged mode amplitudes is the most efficient for the problem in study.

Acknowledgements

505 The authors would like to acknowledge the assistance given by IT Services and the use of the Computational Shared Facility at The University of Manchester. The authors acknowledge the use of ARCHER HPC allocated via UK EPSRC Turbulence Consortium (EPSRC grant EP/L000261/1).

References

- 510 J. Andreopoulos. Initial conditions, Reynolds number effects and the near field characteristics of the round jet in a cross flow. *Zeitschrift fuer Flugwissenschaften und Weltraumforschung*, 8:118–124, 1984. ISSN 0342-068X. URL <http://adsabs.harvard.edu/abs/1984ZF1We...8..118A>.
- 515 Shervin Bagheri. *Analysis and control of transitional shear flows using global modes*. PhD thesis, Royal Institute of Technology, 2010. URL <http://www.diva-portal.org/smash/record.jsf?pid=diva2%252B288180&dswid=-216>.
- 520 Shervin Bagheri, Philipp Schlatter, Peter J. Schmid, and DAN S. Henningson. Global stability of a jet in crossflow. *Journal of Fluid Mechanics*, 624:33, mar 2009. ISSN 0022-1120. doi: 10.1017/S0022112009006053. URL http://journals.cambridge.org/abstract_S0022112009006053.
- 525 G. Bidan and D. E. Nikitopoulos. On steady and pulsed low-blowing-ratio transverse jets. *Journal of Fluid Mechanics*, 714:393–433, jan 2013a. ISSN 0022-1120. doi: 10.1017/jfm.2012.482. URL http://journals.cambridge.org/abstract_S002211201200482X.
- Guillaume Bidan and Dimitris Nikitopoulos. Film-Cooling Jets Analyzed with Proper Orthogonal Decomposition and Dynamic Mode Decomposition. In *43rd Fluid Dynamics Conference*, Reston, Virginia, jun 2013b. American Institute of Aeronautics and Astronautics. ISBN 978-1-62410-214-1. doi: 10.2514/6.2013-2970. URL <http://arc.aiaa.org/doi/10.2514/6.2013-2970>.

- Kevin K. Chen, Jonathan H. Tu, and Clarence W. Rowley. Variants of dynamic mode decomposition: Boundary condition, Koopman, and fourier analyses. *Journal of Nonlinear Science*, 22(6):887–915, dec 2012. ISSN 09388974. doi: 10.1007/s00332-012-9130-9. URL <http://link.springer.com/10.1007/s00332-012-9130-9>.
- Sergio L. V. Coelho and J. C. R. Hunt. The dynamics of the near field of strong jets in crossflows. *Journal of Fluid Mechanics*, 200:95, apr 1989. ISSN 0022-1120. doi: 10.1017/S0022112089000583. URL http://journals.cambridge.org/abstract_S0022112089000583.
- L. Corteleazzi and a. R. Karagozian. On the formation of the counter-rotating vortex pair in transverse jets. *Journal of Fluid Mechanics*, 446:347–373, nov 2001. ISSN 00221120. doi: 10.1017/S0022112001005894. URL <http://www.scopus.com/inward/record.url?eid=2-s2.0-0035841488&partnerID=tZ0tx3y1>.
- Mostafa Esmaeili, Asghar Afshari, and Farhad A. Jaberi. Turbulent mixing in non-isothermal jet in crossflow. *International Journal of Heat and Mass Transfer*, 89:1239–1257, 2015. ISSN 00179310. doi: 10.1016/j.ijheatmasstransfer.2015.05.055.
- T. F. Fric and A. Roshko. Vortical structure in the wake of a transverse jet. *Journal of Fluid Mechanics*, 279:1–47, apr 1994. ISSN 0022-1120. doi: 10.1017/S0022112094003800. URL http://journals.cambridge.org/abstract_S0022112094003800.
- Keinosuke Fukunaga. *Introduction to statistical pattern recognition*. Academic Press, San Diego, 1990. ISBN 9780080478654.
- R. W. Grout, A. Gruber, C. S. Yoo, and J. H. Chen. Direct numerical simulation of flame stabilization downstream of a transverse fuel jet in cross-flow. *Proceedings of the Combustion Institute*, 33(1):1629–1637, 2011. ISSN 15407489. doi: 10.1016/j.proci.2010.06.013.
- Guangbin He, Yanhu Guo, and Andrew T. Hsu. The effect of Schmidt number on turbulent scalar mixing in a jet-in-crossflow. *International Journal of Heat and Mass Transfer*, 42(20):3727–3738, 1999. ISSN 00179310. doi: 10.1016/S0017-9310(99)00050-2.
- Philip Holmes, John L. Lumley, Gahl Berkooz, and Clarence W. Rowley. *Turbulence, Coherent Structures, Dynamical Systems and Symmetry*. Cambridge University Press, Cambridge, 2012. ISBN 9780511919701. doi: 10.1017/CBO9780511919701. URL <http://ebooks.cambridge.org/ref/id/CBO9780511919701>.
- Hector Iacovides, Diamantis Kounadis, Brian E. Launder, Jiankang Li, and Zeyuan Xu. Experimental Study of the Flow and Thermal Development of a Row of Cooling Jets Impinging on a Rotating Concave Surface. *Journal of Turbomachinery*, 127(1):222, 2005. ISSN 0889504X. doi: 10.1115/1.1812778. URL <http://turbomachinery.asmedigitalcollection.asme.org/article.aspx?articleid=1466968&http://www.scopus.com/inward/record.url?eid=2-s2.0-16244422286&partnerID=40&md5=e63cdcb1837801df1e4b7bea94aa7b7c>.
- Miloš Ilak, Philipp Schlatter, Shervin Bagheri, and Dan S. Henningson. Bifurcation and stability analysis of a jet in cross-flow: onset of global instability at a low velocity ratio. *Journal of Fluid Mechanics*, 696:94–121, mar 2012. ISSN 0022-1120. doi: 10.1017/jfm.2012.10. URL http://journals.cambridge.org/abstract_S0022112012000109.
- Prahladh S. Iyer and Krishnan Mahesh. A numerical study of shear layer characteristics of low-speed transverse jets. *Journal of Fluid Mechanics*, 790(10):275–307, mar 2016. ISSN 0022-1120. doi: 10.1017/jfm.2016.7. URL http://www.journals.cambridge.org/abstract_S0022112016000070.
- Mihailo R. Jovanović, Peter J. Schmid, and Joseph W. Nichols. Sparsity-promoting dynamic mode decomposition. *Physics of Fluids*, 26(2):024103, feb 2014. ISSN 1070-6631. doi: 10.1063/1.4863670. URL <http://scitation.aip.org/content/aip/journal/pof2/26/2/10.1063/1.4863670>.
- Sylvain Laizet and Eric Lamballais. High-order compact schemes for incompressible flows: A simple and efficient method with quasi-spectral accuracy. *Journal of Computational Physics*, 228(16):5989–6015, sep 2009. ISSN 00219991. doi: 10.1016/j.jcp.2009.05.010. URL <http://www.sciencedirect.com/science/article/pii/S0021999109002587>.
- Sylvain Laizet and Ning Li. Incompact3d: A powerful tool to tackle turbulence problems with up to O(105) computational cores. *International Journal for Numerical Methods in Fluids*, 67(11):1735–1757, dec 2011. ISSN 02712091. doi: 10.1002/fld.2480. URL <http://doi.wiley.com/10.1002/fld.2480>.
- A. Liakopoulos, P. A. Blythe, and H. Gunes. A reduced dynamical model of convective flows in tall laterally heated cavities. *Proceedings of the Royal Society A: Mathematical, Physical and Engineering Sciences*, 453(1958):663–672, mar 1997. ISSN 1364-5021. doi: 10.1098/rspa.1997.0037. URL <http://rspa.royalsocietypublishing.org/cgi/doi/10.1098/rspa.1997.0037>.
- J. L. Lumley. The Structure of Inhomogeneous Turbulence. In A. M. Yaglom and V. I. Tatarski, editors, *Atmospheric Turbulence and Wave Propagation*, pages 166–178, Nauka, Moscow, 1967. URL <http://www.researchgate.net/publication/248025649>.
- Knudrik E. Meyer, Jakob M. Pedersen, and Oktay Özcan. A turbulent jet in crossflow analysed with proper orthogonal decomposition. *Journal of Fluid Mechanics*, 583:199, jul 2007. ISSN 0022-1120. doi: 10.1017/S0022112007006143.

- 585 URL http://journals.cambridge.org/abstract_S0022112007006143.
 Igor Mezić. Analysis of Fluid Flows via Spectral Properties of the Koopman Operator. *Annual Review of Fluid Mechanics*, 45(1):357–378, jan 2013. ISSN 0066-4189. doi: 10.1146/annurev-fluid-011212-140652. URL <http://www.annualreviews.org/doi/abs/10.1146/annurev-fluid-011212-140652>.
- 590 Tomas W. Muld, Gunilla Efraimsson, and Dan S. Henningson. Flow structures around a high-speed train extracted using Proper Orthogonal Decomposition and Dynamic Mode Decomposition. *Computers and Fluids*, 57:87–97, 2012. ISSN 00457930. doi: 10.1016/j.compfluid.2011.12.012.
- Frank Muldoon and Sumanta Acharya. Direct Numerical Simulation of pulsed jets-in-crossflow. *Computers & Fluids*, 39(10):1745–1773, dec 2010. ISSN 00457930. doi: 10.1016/j.compfluid.2010.04.008. URL <http://www.sciencedirect.com/science/article/pii/S0045793010000848>.
- 595 Suman Muppudi and Krishnan Mahesh. Direct numerical simulation of round turbulent jets in crossflow. *Journal of Fluid Mechanics*, 574:59–84, mar 2007. ISSN 1469-7645. URL http://journals.cambridge.org/abstract_S0022112006004034.
- 600 M. A. Ol'shanskii and V. M. Staroverov. On simulation of outflow boundary conditions in finite difference calculations for incompressible fluid. *International Journal for Numerical Methods in Fluids*, 33(4):499–534, jun 2000. ISSN 0271-2091. doi: 10.1002/1097-0363(20000630)33:4<499::AID-FLD19>3.0.CO;2-7. URL [http://doi.wiley.com/10.1002/1097-0363\(%252820000630%252933%2523A4%2523C499%2523A%2523AAID-FLD19%2523E3.0.CO%2523B2-7](http://doi.wiley.com/10.1002/1097-0363(%252820000630%252933%2523A4%2523C499%2523A%2523AAID-FLD19%2523E3.0.CO%2523B2-7).
- 605 Z. A. Rana, B. Thornber, and D. Drikakis. Transverse jet injection into a supersonic turbulent cross-flow. *Physics of Fluids*, 23(4):046103, apr 2011. ISSN 10706631. doi: 10.1063/1.3570692. URL <http://aip.scitation.org/doi/10.1063/1.3570692>.
- Clarence W. Rowley, Igor Mezić, Shervin Bagheri, Philipp Schlatter, and Dan S. Henningson. Spectral analysis of nonlinear flows. *Journal of Fluid Mechanics*, 641:115–127, dec 2009. ISSN 0022-1120. doi: 10.1017/S0022112009992059. URL http://www.journals.cambridge.org/abstract_S0022112009992059.
- 610 M. Salewski, D. Stankovic, and L. Fuchs. Mixing in circular and non-circular jets in crossflow. *Flow, Turbulence and Combustion*, 80(2):255–283, mar 2008. ISSN 13866184. doi: 10.1007/s10494-007-9119-x. URL <http://link.springer.com/10.1007/s10494-007-9119-x>.
- Peter J. Schmid. Dynamic mode decomposition of numerical and experimental data. *Journal of Fluid Mechanics*, 656:5–28, jul 2010. ISSN 0022-1120. doi: 10.1017/S0022112010001217. URL http://journals.cambridge.org/abstract_S0022112010001217.
- 615 Onofrio Semeraro, Gabriele Bellani, and Fredrik Lundell. Analysis of time-resolved PIV measurements of a confined turbulent jet using POD and Koopman modes. *Experiments in Fluids*, 53(5):1203–1220, nov 2012. ISSN 0723-4864. doi: 10.1007/s00348-012-1354-9. URL <http://link.springer.com/10.1007/s00348-012-1354-9>.
- Jerry W. Shan and Paul E. Dimotakis. Reynolds-number effects and anisotropy in transverse-jet mixing. *Journal of Fluid Mechanics*, 566:47–96, nov 2006. ISSN 1469-7645. doi: 10.1017/S0022112006001224. URL http://journals.cambridge.org/abstract_S0022112006001224.
- S. A. Sherif and R. H. Pletcher. Measurements of the Flow and Turbulence Characteristics of Round Jets in Crossflow. *Journal of Fluids Engineering*, 111(2):165–171, jun 1989. ISSN 00982202. doi: 10.1115/1.3243618. URL <http://fluidsengineering.asmedigitalcollection.asme.org/article.aspx?articleid=1426849>.
- 620 Lawrence Sirovich. Turbulence and the dynamics of coherent structures. Part I: Coherent structures. *Quarterly of Applied Mathematics*, 45(3):561–571, 1987. URL <http://www.jstor.org/stable/43637457>.
- Gilles Tissot, Laurent Cordier, Nicolas Benard, and Bernd R. Noack. Model reduction using Dynamic Mode Decomposition. *Comptes Rendus Mécanique*, 342(6-7):410–416, jun 2014. ISSN 16310721. doi: 10.1016/j.crme.2013.12.011. URL <http://linkinghub.elsevier.com/retrieve/pii/S163107211400103X>.
- 625 Mayank Tyagi and Sumanta Acharya. Large Eddy Simulation of Film Cooling Flow From an Inclined Cylindrical Jet. *Journal of Turbomachinery*, 125(4):734, oct 2003. ISSN 0889504X. doi: 10.1115/1.1625397. URL <http://turbomachinery.asmedigitalcollection.asme.org/article.aspx?articleid=1466677>.
- Zhao Wu, Dominique Laurence, and Imran Afgan. Direct simulation of hot jet in cold channel crossflow with temperature mixing. *Mendeley Data*, v3, 2017a. doi: 10.17632/7nx4prgjzz.3.
- 630 Zhao Wu, Dominique Laurence, and Imran Afgan. Direct numerical simulation of a low momentum round jet in channel crossflow. *Nuclear Engineering and Design*, 313:273–284, mar 2017b. ISSN 00295493. doi: 10.1016/j.nucengdes.2016.12.018. URL <http://linkinghub.elsevier.com/retrieve/pii/S0029549316305040>.
- Zhao Wu, Dominique Laurence, Hector Iacovides, and Imran Afgan. Direct simulation of conjugate heat transfer of jet in channel crossflow. *International Journal of Heat and Mass Transfer*, 110:193–208, jul 2017c. ISSN 00179310. doi: 10.1016/j.ijheatmasstransfer.2017.03.027. URL <http://www.sciencedirect.com/science/article/pii/S0017931016327041> <http://linkinghub.elsevier.com/retrieve/pii/S0017931016327041>.
- 635
- 640